

# JGR Space Physics

## RESEARCH ARTICLE

10.1029/2023JA032013

### Key Points:

- The role of plasmaspheric field-aligned density structure in the formation of electron thermal heat fluxes
- SuperThermal Electron Transport (STET) simulations of thermal heat fluxes using physics-based 3D dynamic Belgian SWIFF Plasmasphere Model (BSPM)
- The BSPM simulation confirms the plasmaspheric field-aligned density structure used in STET code and supports the heat flux calculations

### Correspondence to:

G. V. Khazanov,  
George.V.Khazanov@nasa.gov

### Citation:

Khazanov, G. V., Pierrard, V., Ma, Q., & Botek, E. (2023). The role of plasmasphere in the formation of electron heat fluxes. *Journal of Geophysical Research: Space Physics*, 128, e2023JA032013. <https://doi.org/10.1029/2023JA032013>

Received 21 AUG 2023

Accepted 20 OCT 2023

### Author Contributions:

**Conceptualization:** George V. Khazanov

**Data curation:** Qianli Ma, Edith Botek

**Formal analysis:** George V. Khazanov, Viviane Pierrard

**Investigation:** George V. Khazanov, Qianli Ma

**Methodology:** George V. Khazanov, Viviane Pierrard, Qianli Ma

**Project Administration:** George V. Khazanov

**Resources:** George V. Khazanov

**Software:** George V. Khazanov, Viviane Pierrard, Qianli Ma, Edith Botek

**Supervision:** George V. Khazanov

**Validation:** George V. Khazanov





**Visualization:** Viviane Pierrard, Qianli Ma, Edith Botek

**Writing – original draft:** George V. Khazanov, Viviane Pierrard

**Writing – review & editing:** George V. Khazanov, Viviane Pierrard, Qianli Ma

© 2023 American Geophysical Union. All Rights Reserved. This article has been contributed to by U.S. Government employees and their work is in the public domain in the USA.

## The Role of Plasmasphere in the Formation of Electron Heat Fluxes

George V. Khazanov<sup>1</sup> , Viviane Pierrard<sup>2,3</sup> , Qianli Ma<sup>4,5</sup> , and Edith Botek<sup>2</sup> 

<sup>1</sup>NASA Goddard Space Flight Center, Greenbelt, MD, USA, <sup>2</sup>Royal Belgian Institute for Space Aeronomy, Solar-Terrestrial Center of Excellence (STCE) and Space Physics, Brussels, Belgium, <sup>3</sup>Center for Space Radiations (CSR), Georges Lemaître Center for Earth and Climate Research (TECLIM), Earth and Life Institute (ELI), Université Catholique de Louvain (UC Louvain), Louvain-la-Neuve, Belgium, <sup>4</sup>Center for Space Physics, Boston University, Boston, MA, USA, <sup>5</sup>Department of Atmospheric and Oceanic Sciences, University of California, Los Angeles, CA, USA

**Abstract** Plasmasphere plays an important role in the magnetospheric physics, defining many important inputs to the ionosphere from the middle to the auroral latitudes. Among them are electron thermal heat fluxes resulting from the Coulomb interaction of superthermal electrons (SE) and cold plasmaspheric electrons. These fluxes define the electron temperature at the upper ionospheric altitudes and are the input to the global ionospheric modeling networks. As was previously found from the calculation of lower energy SE and thermal heat fluxes, the knowledge of field-aligned cold plasma distribution in the plasmasphere is a very sensitive parameter that introduces the most uncertainties in the calculation of these values. To verify the previously used SuperThermal Electron Transport code assumptions regarding plasmaspheric field-aligned density structure  $\sim [B(s)/B_0]^a$ , we used the latest version of 3D plasmaspheric model developed by Pierrard, Botek, and Darrouzet (2021, <https://doi.org/10.3389/fspas.2021.681401>). Such an assumption is found to be very reasonable in the calculations of electron thermal heat fluxes entering upper ionospheric altitudes and the associated electron temperature formation for the two selected dayside and nightside electron precipitation events driven by whistler-mode wave activity.

## 1. Introduction

In the classical book by Lemaire and Gringauz (1998), the plasmasphere is defined as the extension of the ionosphere at low-latitude and midlatitude and is filled by low-energy plasma. The plasmasphere usually refers to the high-density region in corotation with the Earth, as opposed to the plasma trough which is the low-density region above the plasmopause (Grebowsky, 1970). In particular, the hiss waves are generally observed in the plasmasphere, while the chorus waves are observed in the plasma trough (e.g., Meredith et al., 2018, 2020). Observations by Cluster and IMAGE (Imager for Magnetopause-to-Aurora Global Exploration) spacecraft have provided a new insight in understanding the plasmasphere formation (Darrouzet et al., 2009) stimulating development of different kinds of plasmaspheric models. In addition to the plasmasphere refilling from the ionosphere, an additional plasmasphere refilling mechanism came recently into focus: charge exchange reactions between ring current ions and exospheric neutral hydrogen atoms (Liu et al., 2022). Empirical and physics-based models have been developed to reproduce the inner region of the magnetosphere and its boundary called the “plasmopause” (see Pierrard et al. (2009) for a review). As was mentioned in recent work by Pierrard, Botek, and Darrouzet (2021), “It is quite difficult to compare all the existing models, since some are purely empirical (e.g., Sheeley et al., 2001), based on data assimilation; some are an amalgam of different analytical relations (e.g., Gallagher et al., 2000), and others more physics-based, e.g., the Dynamic Global Core Plasma Model (DGCPM) of Ober et al. (1997), the fluid model SAMI3 (Huba et al., 2008), or the Ionosphere-Plasmasphere IP model (Maruyama et al., 2016)].” The different physics-based (Mishin & Puhl-Quinn, 2007) and statistical models of plasmopause (Ripoll et al., 2022) and of plasmasphere (Ripoll et al., 2023) were recently reviewed in view of simulating their interactions with the radiation belt particles.

Plasmasphere and lower energy electrons play the important role in the magnetospheric physics (Darrouzet et al., 2009; Ganushkina et al., 2015; Lemaire & Gringauz, 1998; Mishin, 2023). In the connection with our studies presented in this manuscript, we want to emphasize the role of plasmasphere field-aligned density distribution in defining the high-energy electron precipitation to the atmosphere (Khazanov, Ma, & Chu, 2022) and the formation of electron heat fluxes (Khazanov et al., 2023). These two effects are ultimately connected through

magnetosphere-ionosphere coupling processes, providing important feedback to the formation of plasmasphere itself and the overall magnetospheric circulation dynamics.

Electron thermal heat flux that defines electron temperature ( $T_e$ ) at the ionospheric altitudes is basically an unknown parameter and this fact creates some difficulties in ionospheric studies (Bekerat et al., 2007; Glocer et al., 2012, 2017; Richmond et al., 1992; Ridley et al., 2006; Schunk et al., 1986). To explain large  $T_e$  observations at the high-latitude ionosphere reaching 5,000–10,000 K (Curtis et al., 1985; Fontheim et al., 1987; Kofman & Wickwar, 1984) Schunk et al. (1986) suggested that “the high-latitude ionosphere interfaces with the hot, tenuous, magnetospheric plasma, and a heat flow into the ionosphere is expected.” This approach was very useful and led the ionospheric modelers to explain some of electron temperature peculiarities even without knowing the processes that are behind the physics of the electron thermal fluxes formation.

Based on SuperThermal Electron Transport (STET) code, we continue to develop the systematic, first-principal calculation of electron heat fluxes in different space plasma regions that potentially would allow the ionospheric community to set up the physics-based approach in the evaluation of  $T_e$  upper boundary ionospheric conditions. In a past, we applied these studies for the different space plasma regions (Khazanov, 2011; Khazanov et al., 2019, 2020, 2021), and always emphasized the important role of plasmasphere in the study of this phenomena.

The STET code that was used in these calculations for middle and auroral altitudes considered the ionosphere-plasmasphere system as the one interconnected unit with the inclusion of two conjugated and coupled ionospheres in the Northern and Southern hemispheres. Above-mentioned studies for these space plasma regions clearly demonstrated that the electron heat fluxes that are produced using STET code, as a result of Coulomb interaction of photoelectron and secondary electron with cold plasmasphere, depend on the field-aligned plasma density distribution. That means that approach of setting the plasmasphere in the STET code must be validated by using first-principal 3D plasmaspheric modeling networks that naturally produces the field-aligned cold electron density distribution (Huba et al., 2008; Maruyama et al., 2016; Pierrard & Stegen, 2008).

To verify the previously used assumptions regarding plasmaspheric field-aligned density structure, we used the latest version of 3D plasmaspheric model developed by Pierrard, Botek, and Darrouzet (2021) and applied it for the calculation of the selected cases of electron thermal heat fluxes generated by intense whistler-mode waves measured by Van Allen Probes observations (Khazanov, Ma, & Chu, 2022). Compared to plasmasphere modelers, the radiation belt community usually separates “plasmasphere” with “plasma trough” at the magnetic equator using a “plasmopause,” with higher cold electron density in the plasmasphere and lower density in the plasma trough. The energetic electron precipitation is mainly caused by whistler-mode chorus waves in the plasma trough at  $L < 7$ , and hiss waves in the dayside plasmasphere and plumes of the Earth's magnetosphere (Ma et al., 2020, 2021).

This paper has the following organization. Section 2 briefly presents the methodology of electron heat flux calculation using STET code. Section 3 discusses the selection of 3D plasmaspheric model in the calculation of field-aligned cold density structure. The electron heat simulation scenarios that use selected Van Allen Probes observations are presented in Section 4, and the results of electron thermal flux simulations are summarized in Section 5.

## 2. STET Electron Heat Flux Calculation

It is useful to briefly remind the readers about the STET code features and the assumptions used in the past regarding setting of the cold electron distribution in plasmasphere. The Time-Dependent STET code to be used in this paper solves the gyro-average kinetic equation for electron energies above of 1 eV and is well documented (Khazanov, 2011; Khazanov et al., 2021). Applying this kinetic equation for the study of electron heat fluxes presented in this manuscript, this equation is presented as

$$\frac{1}{v} \frac{\partial \Phi}{\partial t} + \mu \frac{\partial \Phi}{\partial s} - \frac{1 - \mu^2}{2} \left( \frac{1}{B} \frac{\partial B}{\partial s} - \frac{F}{E} \right) \frac{\partial \Phi}{\partial \mu} + EF\mu \frac{\partial}{\partial E} \left( \frac{\Phi}{E} \right) = Q + \langle S \rangle \quad (1)$$

where the electron number flux  $\Phi = 2Ef/m^2$  is a function of time ( $t$ ),  $s$  is the distance along the magnetic field,  $\mu$  is the cosine of the pitch angle between the velocity  $v$  and the magnetic field  $B$ ,  $E$  is the electron energy,  $f$  is the

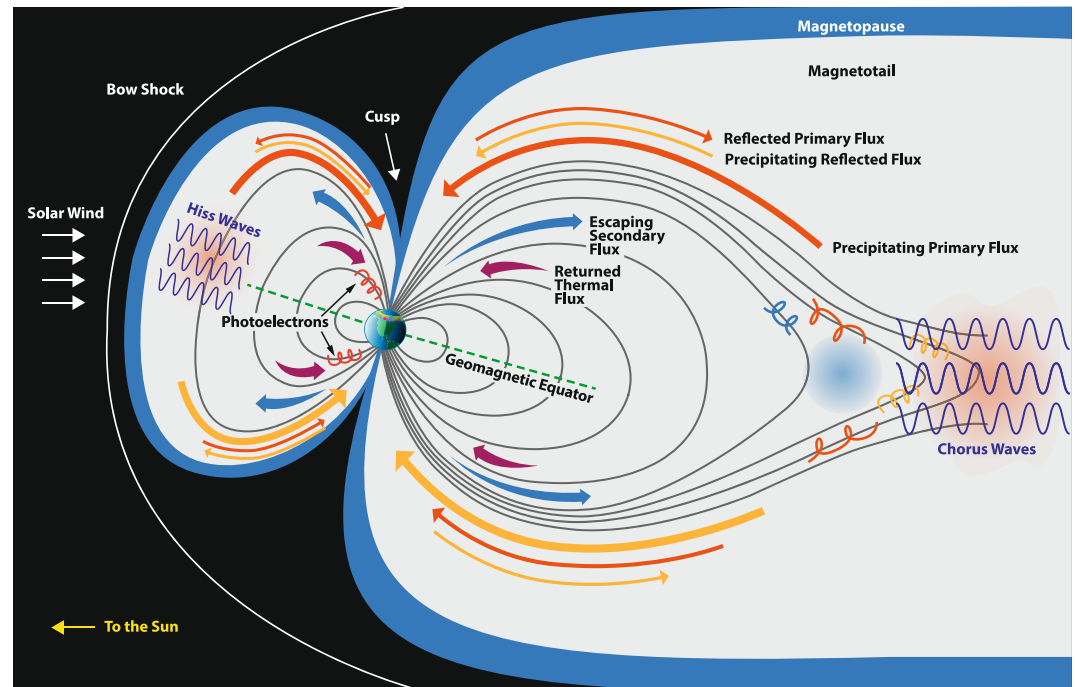


**Figure 1.** Magnetosphere-ionosphere-atmosphere processes included in tilted magnetic dipole geometry of SuperThermal Electron Transport code.

electron phase space density,  $m$  is the electron mass, and  $F$  is the electric field force. The right-hand side represents the source term  $Q$  due to photoionization and the loss term  $\langle S \rangle$  due to the various collisional processes. The collision terms in STET code include elastic collisions between charged and neutral particles, all nonelastic collisions between electrons and neutrals for the electron energies above of 1 eV, and wave-particle interaction (WPI) between the electrons and the whistler-mode waves. STET code can provide the full energy and pitch-angle distribution of superthermal electrons (SE) along the closed magnetic field lines without interruption between the magnetosphere and the ionosphere, thus providing a useful tool to understand the MIA coupling dynamics in the auroral regions. STET is a well-established code developed and improved in the past few decades (see Khazanov (2011), Khazanov et al. (2015), and Khazanov et al. (2020, 2021) for any further details).

To make the proper discussion regarding the plasmaspheric model selection, we further *must* repeat and quote the important STET code setting details that was multiple times discussed in the past in our previous above-mentioned studies. The simulations that are presented below are based on the tilted dipole magnetic field configuration as it is shown in Figure 1. The MSIS-90 model (Hedin, 1991) is used for the neutral atmosphere and cold plasma density distribution in the ionosphere is based on the International Reference Ionosphere (IRI-2016) model (Bilitza et al., 2017). Further, this plasma density structure was extended into the magnetosphere based on the specific assumptions that are discussed in Section 3.

For readers continence, and deep understanding of our approach in the plasmaspheric model selection, we briefly outline our simulation methodology of electron thermal flux calculation presented by Khazanov et al. (2023). The electron heat flux going into the upper ionosphere was calculated using STET-based method presented in Khazanov et al. (2019, 2020). To do this, we integrate the electron-electron and electron-ion collisional terms in the SE kinetic Equation 1 over the velocity space

$$\langle S_{ee} \rangle + \langle S_{ei} \rangle = An_e \left\{ \frac{\partial}{\partial E} \left( \frac{\Phi}{E} \right) + \frac{1}{2E^2} \frac{\partial}{\partial \mu} \left[ (1 - \mu^2) \frac{\partial \Phi}{\partial \mu} \right] \right\} \quad (2)$$

where  $A = 2\pi e^4 \ln \Lambda$ ,  $\ln \Lambda$  is the Coulomb logarithm,  $n_e(s)$  is the thermal plasma density,  $\Phi = \Phi(s, E, \mu)$  is the SE flux that includes (depending on STET code setting) ionospheric photoelectron and secondary electron as well as degraded primary electrons shown in Figure 1 and get the expression of SE energy deposition to the thermal electrons as

$$Q_e(s) = 4\pi An_e(s)[\Phi_0(E_{\min}) - \Phi_0(E_{\max}) + \int_{E_{\min}}^{E_{\max}} \frac{\Phi_0(E)}{E} dE] \quad (3)$$

where  $\Phi_0$  is the SE omnidirectional flux, with integrational limits of  $E_{\min}$  and  $E_{\max}$  are taken to be as 1 eV and 10 keV, respectively.

Integrating Equation 3 along the field line from the geomagnetic equator,  $s_{eq}$ , to the upper ionospheric boundary,  $s_i$ , we find the incoming electron heat flux entering ionospheric altitudes

$$q(s_i) = \int_{s_{eq}}^{s_i} Q_e(s) \frac{B_i}{B(s)} ds \quad (4)$$

As can be seen from Equation 4, the value of  $q(s_i)$  is a function of the density structure above the upper ionospheric altitude of  $s_i$  that in our studies is selected to be 800 km.

### 3. Selection of 3D Plasmasphere Model

The physical mechanisms and their description can vary in different 3D plasmaspheric models, following the theoretical approaches, including the formation of the plasmopause itself. That is why there are many different criteria we used to select the 3D plasmaspheric model to work with. To name just a few of them that are important elements for such a choice: (a) determination of some common features and parameters that are used in both STET code and the corresponding model, (b) availability and flexibility of the corresponding model for specific studies, and (c) the possibility to cross-check and verify the assumptions that each model uses. Not to be mentioned here, there is also a human factor that involved in the selection of certain models to work with.

The latest version of the Belgian Plasmasphere Ionosphere Model (Pierrard, Botek, & Darrouzet, 2021) is also called BSPM (Belgian SWIFF Plasmasphere Model where SWIFF refers to Space Weather Integrated Forecasting Framework (Lapenta et al., 2013)): it is a 3D-kinetic semiempirical model of the plasmasphere and coupled to the ionosphere by means of the IRI model (Bilitza et al., 2017) as boundary condition (Pierrard & Voiculescu, 2011). The BSPM is based on the physical mechanism of interchange instability for the plasmopause formation (Pierrard & Lemaire, 2004) and trajectories of particles trapped in the Earth's magnetic field (Pierrard & Stegen, 2008), to provide the number density and the temperature of the electrons and protons inside and outside the plasmasphere, as well as the position of the plasmopause, as a function of time. The model takes into account the corotation and convection electric fields depending on the geomagnetic activity level and is able to reproduce the plasmaspheric plumes appearing during geomagnetic storms (Pierrard et al., 2008). The equations describing the plasma trough region as a function of the position and geomagnetic activity have been recently improved using new satellite data from the NASA Van Allen Probes mission (Botek et al., 2021). The results of the BSPM model and its previous versions have been validated against different physical processes (Bandic et al., 2020; Lemaire & Pierrard, 2008) and compared to many spacecraft observations: IMAGE (Pierrard & Cabrera, 2006; Pierrard & Stegen, 2008), Cluster (Darrouzet et al., 2013; Verbanac et al., 2015), CRRES (Bandic et al., 2016), THEMIS (Bandic et al., 2017; Verbanac et al., 2018), and Van Allen Probes (Pierrard, Botek, Ripoll, et al., 2021) for instance.

As we noticed in the previous section, STET code uses IRI-2016 model (Bilitza et al., 2017) only at ionospheric altitudes below of 800 km. Above this altitude, it was assumed that the electron density from the ionosphere altitude of 800 km monotonically drops in the magnetosphere as:  $N(s) = N_o * [B(s)/B_o]^a$ , where  $N_o$  and  $B_o$  are electron thermal density and magnetic field at the altitude of 800 km. Below this altitude, we used IRI model. In some of the STET code simulations when analyzing photoelectron distribution function at altitudes of FAST satellite observation (Khazanov et al., 2016) or calculating electron thermal fluxes in the region of diffuse aurora (Khazanov et al., 2020), the values of  $a$  representing the thermal electron density structure in the plasmasphere along the field lines were selected to be  $a = 1, 3/2$ , and 2, representing cases corresponding to the plasmaspheric refilling for  $a = 3/2$  to 2, and the transition to the quiet magnetospheric conditions for  $a = 1$  to  $3/2$ .

Other alternatives of STET code simulation, in the cases when the thermal electron density,  $N_{VA}$ , was available at the equatorial magnetospheric plane from Van Allen Probes (formerly known as Radiation Belt Storm Probes, RBSP) observations (Khazanov et al., 2021, Khazanov, Ma, & Chu, 2022), the parameter  $a$  was found by

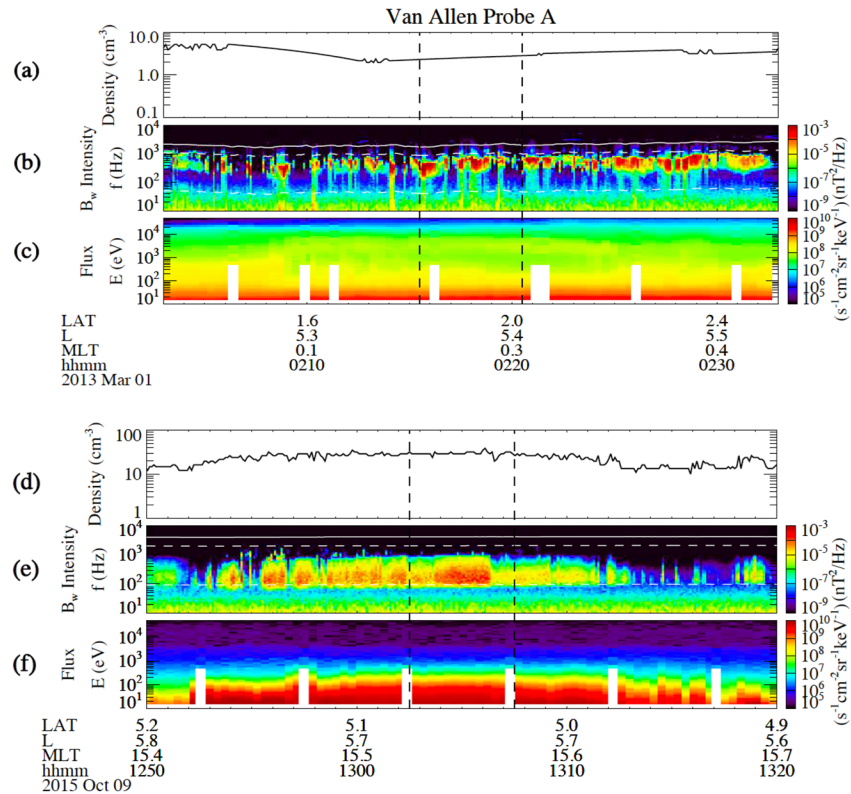


**Figure 2.** Van Allen Probe A observations of chorus (a)–(c) and hiss (d)–(f) modes of the whistler waves and the affiliated plasma parameters on 01 March 2013 and 09 October 2015, correspondingly.

connecting RBSP electron density value from upper hybrid waves measurements and IRI model. In this case, it was assumed that electron density monotonically drops from ionosphere and  $a$  was calculated using the following relation:  $N_{VA} = N_o * [B_{VA}/B_o]^a$ , where  $B_{VA}$  is the magnetic field at RBSP altitude. Such an approach, however, requires some justification because at the L-shells larger or around 4–5, one should expect some of the peculiarities of electron density distribution along the field line related with plasmapause and other plasmaspheric features predicted by dynamic BSPM (Pierrard, Botek, & Darrouzet, 2021).

To do such a validation analysis of our approach, we selected the recent STET code simulations of electron heat formation that was performed by Khazanov, Ma, and Chu (2022) using RBSP observation of intense whistler-mode waves at the night and day magnetospheric sides at the L-shells of around 5–6. Such a selection was not arbitrary because (a) this area is supported by theoretical and experimental plasma temperatures data that was adapted in the plasmaspheric model by Pierrard, Botek, and Darrouzet (2021), and (b) magnetic field line connection of this magnetospheric region with auroral ionospheric latitudes.

Figure 2 shows RBSP observation selection in our studies. The chorus wave event on 01 March 2013 in Figures 2a–2c was observed during the main phase of a modest geomagnetic storm and the hiss wave event on 09 October 2015 in Figures 2d–2f was observed during the recovery phase of the storm. Panels (a) and (d) in this figure show the cold plasma density during these two events, and panels (b, e) and (c, f) show the intensities of whistler-mode waves and electron fluxes at 15 eV–50 keV energies, correspondingly. Here, in Figure 2, we also show 5-min intervals (two dashed vertical lines) during each wave event to perform the electron precipitation analysis that presented below.

Figure 3 presents the observed frequency spectra of chorus and hiss magnetic power intensity and the calculation of local diffusion coefficients for the chorus and hiss waves. These pitch-angle diffusion coefficients are shown as a function of electron energy and pitch angle at 0°, 10°, and 20° magnetic latitudes. The diffusion coefficients are calculated using the observed wave frequency spectrum, quasifield-aligned wave normal angle, and the observed cold electron density and magnetic field. These parameters, along with the observed field-aligned thermal density,



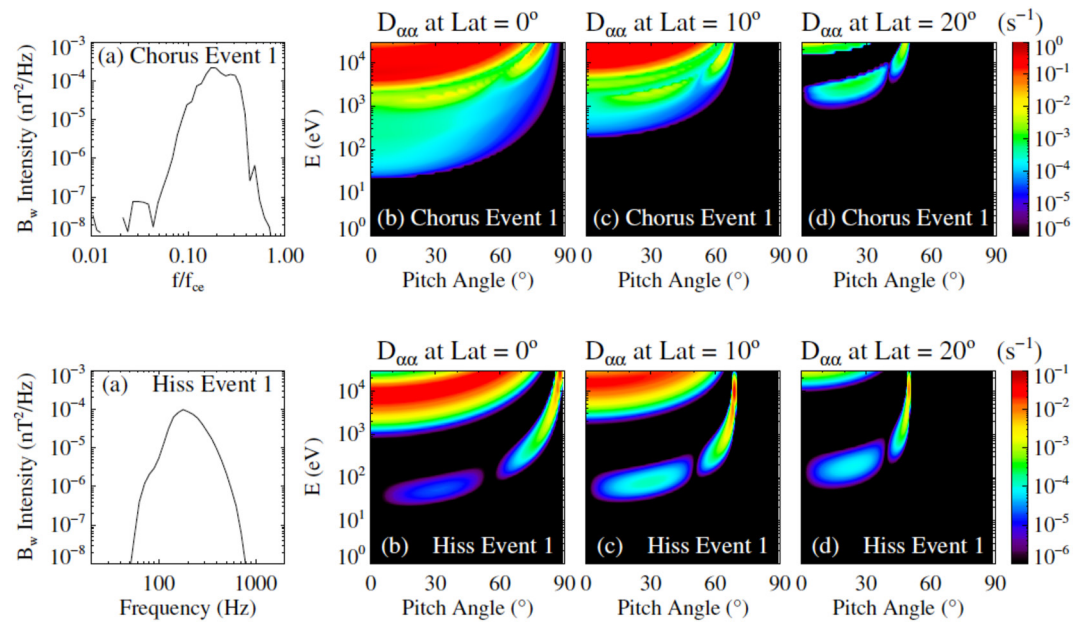


**Figure 3.** Pitch-angle diffusion coefficients calculated for whistler-mode chorus and hiss waves based on the corresponding experimental data of Van Allen Probe A presented in Figure 2.

are used by STET code. We refer readers to the paper by Khazanov, Ma, and Chu (2022) where the additional important details of these two events presented in Figures 2 and 3 were discussed.

As it is shown in Figure 3 and discussed by Khazanov, Ma, and Chu (2022), the magnetospheric whistler-mode waves, chorus and hiss, cannot provide the resonance heating of the low-energy (e.g., cold to 100 eV) electron plasma population with high number fluxes. However, these whistler-mode branches can implicitly participate in the heating processes of plasma thermal electron population by triggering the electron precipitation over a broad energy range (mainly above 1 keV) from the magnetosphere and subsequent atmospheric ionization processes leading to the production of SE population. These SE play a large role in the magnetosphere-ionosphere-atmosphere energy interplay with participation of both magnetically conjugate hemispheres, and their Coulomb interaction with background magnetospheric thermal electrons.

#### 4. Electron Heat Flux Simulation Scenario

Figure 1 presents electron heat flux simulation scenario that was driven by ionospheric photoelectrons and strong whistler-mode waves. Complete discussion of magnetospheric parameters of our studies is presented by Khazanov, Ma, and Chu (2022). Here, we only modified the plasmaspheric setting that correspond to these two cases shown in Figure 4 and provide the brief discussion of the simulation scenario of our analysis just as the reference point.

Figure 4 illustrates the plasmasphere configuration and electron densities predicted using 3D plasmaspheric model (BSPM) by Pierrard, Botek, and Darrouzet (2021) in the equatorial and the meridian planes. The plasmapause position corresponds to the black circles in the equatorial plane. The orange region represents the density in the plasmasphere (red in the ionosphere) while the blue region until 8 Re corresponds to the low-density plasma trough. The left panels illustrate the case of 01 March 2013 at 2 hr UT. The small black crosses correspond to the magnetic field line  $L = 5.4$ . Due to the increase of Bartels geomagnetic index  $K_p$  to 5 (see top panel), a plume is generated that extends up to 8 Re in the noon sector (the Sun is located at the left of the figures), while on the contrary, the plasmapause is located quite close to the Earth ( $\sim 3.5$  Re) in the postmidnight sector. The right panels correspond to 09 October 2015 at 13hr UT. The small black crosses show the magnetic field line  $L = 5.7$ . The index  $K_p$  is also increasing (up to  $4^+$  at 13 hr), but the plume will be formed only a few hours later. The plasmapause is also quite asymmetric, reaching  $\sim 3$  Re in the postmidnight sector and  $\sim 4.3$  Re in the dawn sector (top of the equatorial figure).

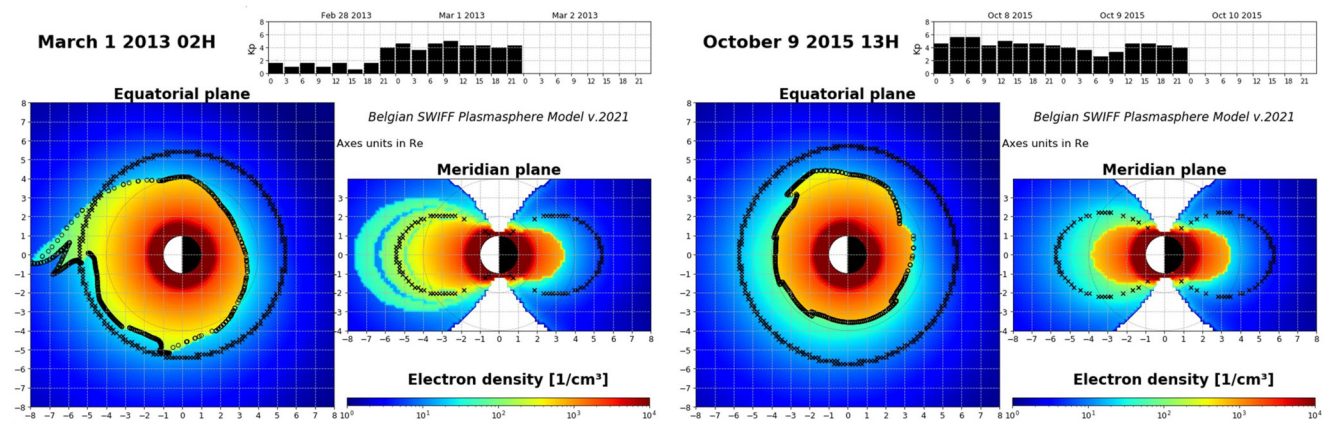


**Figure 4.** Electron density structure predicted using 3D plasmaspheric model (BSPM) by Pierrard, Botek, and Darrouzet (2021) in the equatorial and the meridian plane for 01 March 2013 at 2 hr UT (left panels) and 9 October 2015 at 13 hr UT (right panels).

Strong whistler-mode waves in the equatorial plane of magnetosphere interact with the trapped electron fluxes and create the electron precipitations into the loss-cone. Parameters of these waves, chorus and hiss, are shown in Figures 2 and 3. As we discussed in the previous STET code settings (Khazanov et al., 2023; Khazanov, Ma, & Chu, 2022) “these fluxes are denoted in this figure as the *Precipitating Primary Fluxes* (large red and yellow arrows in Figure 1), have pure magnetospheric origin, and deliver their energy to both Northern and Southern magnetically conjugate regions at the same time. As it was discussed in our previous studies, some of the primary electrons that precipitate into the atmosphere are backscattered into the magnetosphere and are denoted as the *Primary Reflected Flux* in Figure 1. Impact ionization and collisions with neutrals cause the energy degradation of the primary electrons and the production of secondary electrons. The mixed population of primary and secondary (denoted as *Escaping Secondary Flux* (blue arrows in Figure 1)) electrons cascade toward lower energies and escape to the magnetospheric altitudes.”

When these primary reflected and escaping secondary electrons move back inside the loss-cone to the magnetosphere, passing the region of intense whistler-mode wave activity, some of these electrons are scattered back to the trap zone, become trapped by the magnetic field and move between the magnetic point of reflections continually losing their energy colliding with the thermal electron populations, forming so-called *Returned Thermal Flux* that is shown in Figure 1 by purple arrow. Some of these primary reflected and escaping secondary electrons that ended up in the geomagnetic trap can be scattered back to the loss-cone and travel back and forth between the two magnetically conjugate regions, repeating these passes in the velocity and configurational spaces multiple times till they completely lose their energy.

Figure 5a shows calculation of electron heat fluxes using field-aligned cold plasma distribution from our previous studies (Khazanov, Ma, & Chu, 2022) with notations of WPI + PHG and PHG. The notations of WPI + PHV and PHV correspond to heat flux calculation using Pierrard, Botek, and Darrouzet (2021) 3D plasmaspheric model. These cases include chorus waves with characteristics presented in Figures 2 and 3. Histograms with notations of WPI + PHG and WPI + PHV include both sources for the electron heat fluxes: SE precipitated electron fluxes driven by chorus waves and photoelectrons that are produced via interaction of solar UV and X-ray radiations with the neutral atmosphere. The cases with only photoelectron source, PHG and PHV, are presented only for the reference purposes. Their intensities are very low because the zenith angles in the Northern and Southern hemispheres are 133° and 101°, correspondingly, representing the nighttime conditions in the magnetically conjugate regions.

The reason we presented here separately photoelectron heat flux source is because this parameter, besides solar conditions of illumination, exclusively defines the field-aligned electron density structure, presented in the calculation steps given by relations of Equations 2–4. The fact that PHG and PHV cases are practically identical, demonstrates that our assumption regarding representation of plasmaspheric structure as  $N(s) = N_0 * [B(s)/B_0]^a$  (Khazanov, Ma, & Chu, 2022) is reasonable. Besides, these results indicate excellent comparison of selected plasmaspheric model by Pierrard, Botek, and Darrouzet (2021) with the thermal density of RBSP observations. The

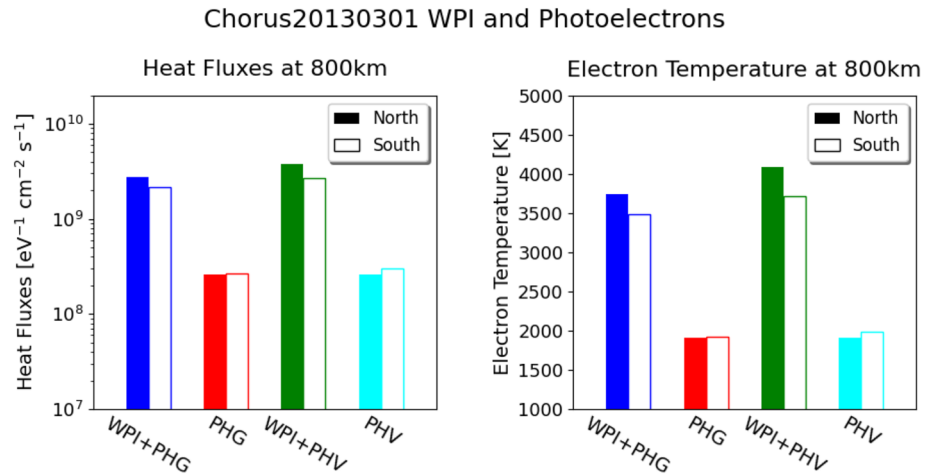


**Figure 5.** Electron thermal heat fluxes and affiliated electron temperature during the event with the presence of chorus waves. We compare the results at Northern and Southern hemispheres from four models: photoelectron production using previous density profile in Khazanov, Gabrielse, et al. (2022) (PHG), photoelectron production using the density profile from 3D plasmaspheric model in Pierrard, Botek, and Darrouzet (2021) (PHV), wave-particle interaction (WPI) and PHG, and WPI + PHV.

proper selection of plasmaspheric temperatures in 3D model (Pierrard & Voiculescu, 2011) was also an important element contributed to successful comparison of this model with different kinds of plasmaspheric observations (Kotova et al., 2018). The BSPM model was recently used to compare the positions of the plasmapause with the boundaries of the auroral oval and the radiation belts (Pierrard, Botek, Ripoll, et al., 2021), and in the past with suboval auroral spots (Yahnin et al., 2013) and spatiotemporal structures of poloidal Alfvén waves detected by Cluster adjacent to the dayside plasmapause (Schäfer et al., 2008). It was also used to calculate the diffusion coefficients of WPIs to determine the influence of the cold plasmaspheric population on the radiation belt particles (Dahmen et al., 2022).

In Figure 5b, using the relation between electron temperatures,  $T_e$ , and electron heat fluxes (see chapter 6 in the book by Khazanov (2011)), we estimate  $T_e$  at the upper ionospheric altitudes of 800 km for selected heat flux cases that are shown in Figure 5a. Electron temperatures that are shown in Figure 5b are in line with the nightside experimental  $T_e$  data that has been discussed and used by Pierrard and Voiculescu (2011).

Now, let us move to the day side of magnetosphere and consider results of STET heat flux simulation in the combination of the hiss wave activity that are shown in Figures 2 and 3 and photoelectrons. These results are presented in Figure 6 and have the same notations as Figure 5. Titles of these plots, however, clearly indicate differences in selected wave activity. Results that presented in Figure 6 that include photoelectrons only are also almost identical indicating similarities in the field-aligned structure between 3D plasmaspheric model and approach by Khazanov, Ma, and Chu (2022). As a result of this, like in the previous chorus wave case, the electron temperatures in Figures 5b and 6b have the same values. The values of the electron heat fluxes in these photoelectron cases are larger because both Northern and Southern hemispheres were illuminated with zenith angles of 65° and 67°, correspondingly.

Results presented in Figures 5 and 6, when both wave activity and photoelectrons are included in the calculation of electron heat fluxes, WPI + PHG and WPI + PHV, show some differences in the calculation of these parameters and corresponding electron temperatures. In the case of chorus waves, the heat flux difference reaches 25% and electron temperatures about 8%. When hiss waves are included in the calculation of these parameters, the uncertainties in the calculations of corresponding values are ~10% and 4%, respectively. For such kind of calculations that are presented in this manuscript, these differences between above-mentioned parameters are reasonable. In the case of the whistler-mode wave activities, the field-aligned density structure enters in the calculation of pitch-angle diffusion coefficients presented in Figure 3 that drive electron precipitation dynamics to begin with. The follow up simulation scenario, presented in Figure 1, ends by the calculation of electron heat flux values by Equations 2–4 that also is a function of the field-aligned density structure. Apparently, these two-step



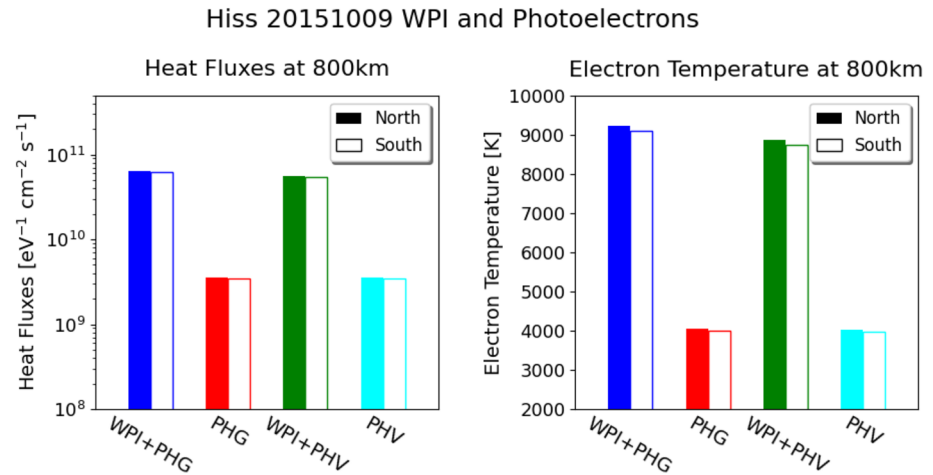


**Figure 6.** Electron thermal heat fluxes and affiliated electron temperature during the event with the presence of the hiss waves.

processes introduce an additional, but small, uncertainty in the analysis of values presented in Figures 5 and 6 for the considered cases of WPI + PHG and WPI + PHV.

The comparison between Figures 5 and 6 suggests that the electron heat fluxes at the dayside is more than 1 order of magnitude higher than those at the nightside, and the electron temperatures at the dayside are more than a factor of 2 higher than the temperatures at the nightside. This difference is partly driven by the different production of sun-lit photoelectron fluxes (see the “PHG” and “PHV” model results in Figures 5 and 6). The magnetospheric conditions and processes also control the electron heat fluxes and temperatures. The pitch-angle scattering rates due to chorus are overall higher than hiss (Figure 3), and the energetic electron fluxes at energies above 1 keV are higher at the nightside than at the dayside (Figures 2b and 2e). However, the cold electron density is higher during the hiss wave event, and there is a significant electron flux enhancement at energies below 200 eV when hiss waves are intensified (Figures 2d–2f). The observed higher SE fluxes during dayside hiss wave event than nightside chorus wave event qualitatively agree with our modeling results at lower energies. The Van Allen Probes could not detect the electron flux profile below ~15 eV energies to directly measure the electron heat flux and temperature, which are only shown in our modeling results.

## 5. Summary and Discussion

Plasmasphere plays an important role in the magnetospheric physics (Darrouzet et al., 2009; Lemaire & Gringauz, 1998; Mishin, 2013, 2023). We want to emphasize in this manuscript the role of the plasmasphere field-aligned density distribution in defining the high-energy electron precipitation to the atmosphere (Khazanov, Ma, & Chu, 2022) and the formation of electron heat fluxes (Khazanov et al., 2023). As it was previously discussed in our studies, “the thermal electron heat flux at the upper ionospheric boundaries is the Achilles’ heel of all global ionospheric models. Such a thermal heat flux setting is especially difficult to justify in the auroral region that is connected to a large energy reservoir of electrons with energies of a few kiloelectron volts, the Earth’s plasma sheet, where MI coupling processes are strongly interconnected.” All these effects are ultimately associated with magnetosphere-ionosphere coupling processes, providing important feedback to the formation of plasmasphere itself and the overall magnetospheric circulation dynamics.

Field-aligned plasmaspheric structure plays an important role in the formation of electron thermal fluxes (Khazanov et al., 2020) and standing along SE calculations (Khazanov et al., 2016), while some assumptions are required regarding cold plasma distribution along geomagnetic field lines. For example, in the study by Khazanov, Ma, and Chu (2022), it was assumed that the electron density from the ionosphere, 800 km, monotonically drops in the magnetosphere as:  $N(s) = N_0 * [B(s)/B_0]^a$ , where  $N_0$  and  $B_0$  are electron thermal density and magnetic field at the altitude of 800 km, respectively. Parameter  $a$  was calculated using IRI-2016 model (Bilitza et al., 2017) at 800 km and the observed electron density value from upper hybrid waves measurements by Van Allen Probes near geomagnetic equator.

To validate our assumption regarding field-aligned density structure, this manuscript uses 3D plasmaspheric model by Pierrard, Botek, and Darrouzet (2021) and applies it to study two Van Allen Probes cases previously analyzed by Khazanov, Ma, and Chu (2022) to calculate electron thermal heat fluxes driven by whistler-mode chorus and hiss waves. As it was demonstrated above, our previously published results are perfectly in line with more sophisticated plasmaspheric density calculation that offers the dynamic BSPM (Pierrard, Botek, & Darrouzet, 2021). Interestingly to notice here that the empirical electron temperature values that are used in this model is consistent with electron temperature calculations presented in this paper.

The fact that the case studies of PHG and PHV, presented in Figures 5 and 6 are practically identical, clearly demonstrates that our assumption regarding representation of plasmaspheric structure as  $N(s) = N_0 * [B(s)/B_0]^a$  (Khazanov, Ma, & Chu, 2022) is reasonable. These results also indicate an excellent comparison of selected plasmaspheric model by Pierrard, Botek, and Darrouzet (2021) with the thermal density of Van Allen Probes observations.

Pitch-angle scattering by whistler-mode waves plays the major role of energetic electron precipitation in the inner magnetosphere. The two events analyzed in our paper are representative examples of chorus-driven electron precipitation at the nightside and hiss-driven precipitation at the dayside. Ma et al. (2020, 2021) performed surveys of the electron precipitation by chorus and hiss waves using Van Allen Probes observation and quasilinear modeling. The location, background conditions, wave characteristics, and trapped electron fluxes for the high precipitating electron fluxes in the statistics are similar to those shown in the two events analyzed in our paper. In addition, the calculated heat fluxes and electron temperatures by STET code are in agreement with radar  $T_e$  observations during one of the substorms across Canada and Alaska (Khazanov, Gabrielse, et al., 2022), and the thermal electron heat flux and electron temperature formation analyzed on a global scale using precipitated auroral electrons measured by three Defense Meteorological Satellite Program (DMSP) satellites during Saint Patrick's 2013 and 2015 Geomagnetic Storms (Khazanov et al., 2023).

Our modeling results suggest that the electron heat flux and temperature are significantly higher in the dayside high-density plasmasphere than the nightside low-density region. The higher cold electron density, higher electron fluxes at tens of eV to 200 eV energies in the magnetosphere, and more efficient photoelectron production at the dayside plasmasphere than the nightside contribute to the higher electron heat flux and temperature from the ionosphere. This result qualitatively agrees with the trend of SE fluxes observed by Van Allen Probes, although the satellite cannot measure the electron fluxes at energies below  $\sim 15$  eV.

Finally, we want to emphasize that chorus and hiss waves have never been discussed by ionospheric and magnetospheric cold plasma modeling communities as the heating source of background electrons. These whistler-mode waves, however, implicitly, and very actively participate in these heating processes, initiation high-energy, keVs electron precipitation that produces the secondary electron populations with the energies of below of 100 eV. Further, the Coulomb collisional processes between the secondary and cold background electrons provide substantial energy input to ionosphere-plasmasphere system. This conclusion is a fundamental outcome of our current and previous study by Khazanov, Ma, and Chu (2022) that now is confirmed with field-aligned thermal density structure simulated by 3D plasmaspheric model developed by Pierrard, Botek, and Darrouzet (2021).

#### Acknowledgments

G.V.K. was partly supported by NASA HTMS program under award of 80NSSC20K1276, the MARBLE Project, funded by the NASA Living with a Star (LWS) Strategic Capabilities program, LWS Program under the award 80NSSC20K1817, NASA award 80NSSC21K1552 and the Comprehensive Auroral Precipitation Experiment (CAPE) on NASA's Geospace Dynamics Constellation (GDC) mission as part of the LWS program. Q.M. was supported by the NASA Grant 80NSSC20K0196 and NSF Grant AGS-2225445. VP and EB thank (a) the project 21GRD02 BIOSPHERE that has received funding from the European Partnership on Metrology, cofinanced by the European Union's Horizon Europe Research and Innovation Programme and by the Participating States, and (b) Horizon 2020 PITHIA-NRF with Grant Agreement 101007599.

#### Data Availability Statement

The authors acknowledge the Van Allen Probes data from the EMFISIS instrument obtained from <http://emfisis.physics.uiowa.edu/Flight/>, and data from the ECT instrument suite obtained from [https://rbsp-ect.newmexicoconsortium.org/data\\_pub](https://rbsp-ect.newmexicoconsortium.org/data_pub). The Belgian plasmasphere BSPM model is available at the ESA (European Space Agency) Virtual Space Weather Modeling Center (<https://swe.ssa.esa.int/kul-cmpa-federated>) and on the PITHIA platform (<https://esc.pithia.eu>) through on-demand executions.

#### References

- Bandic, M., Verbanac, G., Moldwin, M., Pierrard, V., & Piredda, G. (2016). MLT dependence in the relationship between plasmopause, solar wind and geomagnetic activity based on CRRES: 1990–1991. *Journal of Geophysical Research: Space Physics*, *121*, 4397–4408. <https://doi.org/10.1002/2015JA022278>
- Bandic, M., Verbanac, G., & Pierrard, V. (2020). Relationship between global plasmopause characteristics and plasmopause structures in the frame of interchange instability mechanism. *Journal of Geophysical Research: Space Physics*, *125*, e2019JA026768. <https://doi.org/10.1029/2019JA026768>

- Bandic, M., Verbanac, G., Pierrard, V., & Cho, J. (2017). Evidence of MLT propagation of the plasmopause inferred from THEMIS data. *Journal of Atmospheric and Solar-Terrestrial Physics*, *161*, 55–63. <https://doi.org/10.1016/j.jastp.2017.05.005>
- Bekerat, H. A., Schunk, R. W., & Scherliess, L. (2007). Estimation of the high-latitude topside electron heat flux using DMSP plasma density measurements. *Journal of Atmospheric and Solar-Terrestrial Physics*, *69*(9), 1029–1048. <https://doi.org/10.1016/j.jastp.2007.03.015>
- Bilitza, D., Altadill, D., Truhlik, V., Shubin, V., Galkin, I., Reinisch, B., & Huang, X. (2017). International reference ionosphere 2016: From ionospheric climate to real-time weather predictions. *Space Weather*, *15*, 418–429. <https://doi.org/10.1002/2016SW001593>
- Botek, E., Pierrard, V., & Darrouzet, F. (2021). Assessment of the Earth's cold plasmatrrough modeling by using Van Allen Probes/EMFISIS and Arase/PWE electron density data. *Journal of Geophysical Research: Space Physics*, *126*, e2021JA029737. <https://doi.org/10.1029/2021JA029737>
- Curtis, S. A., Hoegy, W. R., Brace, L. H., & Winningham, J. D. (1985). Cusp altitudinal electron temperature gradient: Dynamics Explorer 2 implications for heating mechanisms. *Journal of Geophysical Research*, *90*(A5), 4415–4419. <https://doi.org/10.1029/JA090iA05p04415>
- Dahmen, N., Sicard, A., Brunet, A., Santolik, O., Pierrard, V., Botek, E., et al. (2022). FARWEST: Efficient computation of wave-particle interactions for a dynamic description of the electron radiation belt diffusion. *Journal of Geophysical Research: Space Physics*, *127*, e2022JA030518. <https://doi.org/10.1029/2022JA030518>
- Darrouzet, F., De Keyser, J., & Pierrard, V. (Eds.). (2009). *The Earth's plasmasphere: Cluster and IMAGE—A modern perspective*. Springer. <https://doi.org/10.1007/978-1-4419-1323-4>
- Darrouzet, F., Pierrard, V., Benck, S., Lointier, G., Cabrera, J., Borremans, K., et al. (2013). Links between the plasmopause and the radiation belts boundaries as observed by the instruments CIS, RAPID and WHISPER on CLUSTER. *Journal of Geophysical Research: Space Physics*, *118*, 4176–4188. <https://doi.org/10.1002/jgra.50239>
- Fontheim, E., Brace, L., & Winningham, J. (1987). Properties of low-energy electron precipitation in the cleft during periods of unusually high ambient electron temperatures. *Journal of Geophysical Research*, *92*(A11), 12267–12273. <https://doi.org/10.1029/JA092iA11p12267>
- Gallagher, D. L., Craven, P. D., & Comfort, R. H. (2000). Global core plasma model. *Journal of Geophysical Research*, *105*(A8), 18819–18833. <https://doi.org/10.1029/1999JA000241>
- Ganushkina, N. Y., Amariutei, O. A., Welling, D., & Heynderickx, D. (2015). Nowcast model for low energy electrons in the inner magnetosphere. *Space Weather*, *13*, 16–34. <https://doi.org/10.1002/2014SW001098>
- Glocer, A., Khazanov, G., & Liemohn, M. (2017). Photoelectrons in the quiet polar wind. *Journal of Geophysical Research: Space Physics*, *122*, 6708–6726. <https://doi.org/10.1002/2017ja024177>
- Glocer, A., Kitamura, N., Toth, G., & Gombosi, T. (2012). Modeling solar zenith angle effects on the polar wind. *Journal of Geophysical Research*, *117*, A04318. <https://doi.org/10.1029/2011JA017136>
- Grebowsky, J. M. (1970). Model study of plasmopause motion. *Journal of Geophysical Research*, *75*(22), 4329–4333. <https://doi.org/10.1029/JA075i022p04329>
- Hedin, A. E. (1991). Extension of the MSIS thermospheric model into the middle and lower atmosphere. *Journal of Geophysical Research*, *96*(A2), 1159–1172. <https://doi.org/10.1029/90JA02125>
- Huba, J. D., Joyce, G., & Krall, J. (2008). Three-dimensional equatorial spread F modeling. *Geophysical Research Letters*, *35*, L10102. <https://doi.org/10.1029/2008GL033509>
- Khazanov, G. V. (2011). Kinetic theory of inner magnetospheric plasma. In *Astrophysics and Space Science Library* (Vol. 372, p. 584). Springer Science & Business Media.
- Khazanov, G. V., Chen, M. W., Mishin, E. V., & Chu, M. (2023). Thermal electron heat fluxes associated with precipitated auroral electrons during the Saint Patrick's Days 2013 and 2015 geomagnetic storms. *Journal of Geophysical Research: Space Physics*, *128*, e2022JA031197. <https://doi.org/10.1029/2022JA031197>
- Khazanov, G. V., Gabrielse, C., Glocer, A., Chu, M., Nishimura, Y., & Reyes, P. (2022). A 2D kaleidoscope of electron heat fluxes driven by auroral electron precipitation. *Geophysical Research Letters*, *49*, e2022GL100912. <https://doi.org/10.1029/2022GL100912>
- Khazanov, G. V., Glocer, A., & Chu, M. (2020). The formation of electron heat flux in the region of diffuse aurora. *Journal of Geophysical Research: Space Physics*, *125*, e2020JA028175. <https://doi.org/10.1029/2020JA028175>
- Khazanov, G. V., Glocer, A., & Chu, M. (2021). Electron energy interplay in the geomagnetic trap below the auroral acceleration region. *Journal of Geophysical Research: Space Physics*, *126*, e2020JA028811. <https://doi.org/10.1029/2020JA028811>
- Khazanov, G. V., Himwich, E. W., Glocer, A., & Sibeck, D. (2016). The role of multiple atmospheric reflections in the formation of the electron distribution function in the diffuse aurora region. In *Auroral Dynamics and Space Weather* (pp. 115–130). AGU Monograph
- Khazanov, G. V., Ma, Q., & Chu, M. (2022). Electron heat fluxes generated by intense whistler waves at the upper ionospheric altitudes. *Journal of Geophysical Research: Space Physics*, *127*, e2022JA030753. <https://doi.org/10.1029/2022JA030753>
- Khazanov, G. V., Sibeck, D. G., & Zesta, E. (2019). The formation of electron heat flux over the sunlit quiet polar cap ionosphere. *Geophysical Research Letters*, *46*, 10201–10208. <https://doi.org/10.1029/2019GL084522>
- Khazanov, G. V., Tripathi, A. K., Sibeck, D., Himwich, E., Glocer, A., & Singhal, R. P. (2015). Electron distribution function formation in regions of diffuse aurora. *Journal of Geophysical Research: Space Physics*, *120*, 9891–9915. <https://doi.org/10.1002/2015JA021728>
- Kofman, W., & Wickwar, V. B. (1984). Very high electron temperatures in the daytime F region at Sondrestrom. *Geophysical Research Letters*, *11*(9), 919–922. <https://doi.org/10.1029/GL011i009p00919>
- Kotova, G. M., Verigin, J., Lemaire, V., Pierrard, V., Bezrukh, J., & Smilauer, J. (2018). Experimental study of the plasmasphere boundary layer using MAGION 5 data. *Journal of Geophysical Research: Space Physics*, *123*, 1251–1259. <https://doi.org/10.1002/2017JA024590>
- Lapenta, G., Pierrard, V., Poedts, S., Sebek, O., Travnicek, P. M., Henri, P., et al. (2013). SWIFF: Space weather integrated forecasting framework. *Journal of Space Weather and Space Climate*, *3*, A05. <https://doi.org/10.1051/swsc/2013027>
- Lemaire, J., & Gringauz, K. I. (1998). *The Earth's plasmasphere*. Cambridge University Press. <https://doi.org/10.1017/CBO9780511600098>
- Lemaire, J., & Pierrard, V. (2008). Comparison between two theoretical mechanisms for the formation of the plasmopause and relevant observations. *Geomagnetism and Aeronomy*, *48*(5), 553–570. <https://doi.org/10.1134/S0016793208050010>
- Liu, J., Ilie, R., Borovsky, J. E., & Liemohn, M. W. (2022). A new mechanism for early-time plasmaspheric refilling: The role of charge exchange reactions in the transport of energy and mass throughout the ring current-plasmasphere system. *Journal of Geophysical Research: Space Physics*, *127*, e2022JA030619. <https://doi.org/10.1029/2022JA030619>
- Ma, Q., Connor, H. K., Zhang, X.-J., Li, W., Shen, X.-C., Gillespie, D., et al. (2020). Global survey of plasma sheet electron precipitation due to whistler mode chorus waves in Earth's magnetosphere. *Geophysical Research Letters*, *47*, e2020GL088798. <https://doi.org/10.1029/2020GL088798>
- Ma, Q., Li, W., Zhang, X.-J., Bortnik, J., Shen, X.-C., Connor, H. K., et al. (2021). Global survey of electron precipitation due to hiss waves in the Earth's plasmasphere and plumes. *Journal of Geophysical Research: Space Physics*, *126*, e2021JA029644. <https://doi.org/10.1029/2021JA029644>

- Maruyama, N., Sun, Y.-Y., Richards, P. G., Middlecoff, J., Fang, T.-W., Fuller-Rowell, T. J., et al. (2016). A new source of the midlatitude ionospheric peak density structure revealed by a new ionosphere-plasmasphere model. *Geophysical Research Letters*, *43*, 2429–2435. <https://doi.org/10.1002/2015GL067312>
- Meredith, N. P., Horne, R. B., Kersten, T., Li, W., Bortnik, J., Sicard, A., & Yearby, K. H. (2018). Global model of plasmaspheric hiss from multiple satellite observations. *Journal of Geophysical Research: Space Physics*, *123*, 4526–4541. <https://doi.org/10.1029/2018JA025226>
- Meredith, N. P., Horne, R. B., Shen, X.-C., Li, W., & Bortnik, J. (2020). Global model of whistler mode chorus in the near-equatorial region ( $|\lambda| < 18^\circ$ ). *Geophysical Research Letters*, *47*, e2020GL087311. <https://doi.org/10.1029/2020GL087311>
- Mishin, E. (2013). Interaction of substorm injections with the subauroral geospace: I. Multispacecraft observations of SAID. *Journal of Geophysical Research: Space Physics*, *118*, 5782–5796. <https://doi.org/10.1002/jgra.50548>
- Mishin, E. (2023). The evolving paradigm of the subauroral geospace. *Frontiers in Astronomy and Space Sciences*, *10*, 1118758. <https://doi.org/10.3389/fspas.2023.1118758>
- Mishin, E., & Puhl-Quinn, P. (2007). SAID: Plasmaspheric short circuit of substorm injections. *Geophysical Research Letters*, *34*, L24101. <https://doi.org/10.1029/2007GL031925>
- Ober, D. M., Horwitz, J. L., & Gallagher, D. L. (1997). Formation of density troughs embedded in the outer plasmasphere by subauroral ion drift events. *Journal of Geophysical Research*, *102*(A7), 14595–14602. <https://doi.org/10.1029/97JA01046>
- Pierrard, V., Botek, E., & Darrouzet, F. (2021). Improving predictions of the 3D dynamic model of the plasmasphere. *Frontiers in Astronomy and Space Sciences*, *8*, 681401. <https://doi.org/10.3389/fspas.2021.681401>
- Pierrard, V., Botek, E., Ripoll, J.-F., Thaller, S. A., Moldwin, M. B., Ruohoniemi, M., & Reeves, G. (2021). Links of the plasmopause with other boundary layers of the magnetosphere: Ionospheric convection, radiation belts boundaries, auroral oval. *Frontiers in Astronomy and Space Sciences*, *8*, 728531. <https://doi.org/10.3389/fspas.2021.728531>
- Pierrard, V., & Cabrera, J. (2006). Dynamical simulations of plasmopause deformations. *Space Science Reviews*, *122*(1–4), 119–126. <https://doi.org/10.1007/s11214-005-5670-8>
- Pierrard, V., Goldstein, J., André, N., Jordanova, V. K., Kotova, G. A., Lemaire, J. F., et al. (2009). Recent progress in physics-based models of the plasmasphere. *Space Science Reviews*, *145*(1–2), 193–229. <https://doi.org/10.1007/s11214-008-9480-7>
- Pierrard, V., Khazanov, G., Cabrera, J., & Lemaire, J. (2008). Influence of the convection electric field models on predicted plasmopause positions during the magnetic storms. *Journal of Geophysical Research*, *113*, A08212. <https://doi.org/10.1029/2007JA012612>
- Pierrard, V., & Lemaire, J. (2004). Development of shoulders and plumes in the frame of the interchange instability mechanism for plasmopause formation. *Geophysical Research Letters*, *31*, L05809. <https://doi.org/10.1029/2003GL018919>
- Pierrard, V., & Stegen, K. (2008). A three-dimensional dynamic kinetic model of the plasmasphere. *Journal of Geophysical Research*, *113*, A10209. <https://doi.org/10.1029/2008JA013060>
- Pierrard, V., & Voiculescu, M. (2011). The 3D model of the plasmasphere coupled to the ionosphere. *Geophysical Research Letters*, *38*, L12104. <https://doi.org/10.1029/2011GL047767>
- Richmond, A. D., Ridley, E. C., & Roble, R. G. (1992). A thermosphere/ionosphere general circulation model with coupled electrodynamic. *Geophysical Research Letters*, *19*(6), 601–604. <https://doi.org/10.1029/92GL00401>
- Ridley, A. J., Deng, Y., & Toth, G. (2006). The global ionosphere-thermosphere model. *Journal of Atmospheric and Solar-Terrestrial Physics*, *68*(8), 839–864. <https://doi.org/10.1016/j.jastp.2006.01.008>
- Ripoll, J.-F., Pierrard, V., Cunningham, G. S., Chu, X., Sorathia, K. A., Hartley, D. P., et al. (2023). Modeling of the cold electron plasma density for radiation belt physics. *Frontiers in Astronomy and Space Sciences*, *10*, 1096595. <https://doi.org/10.3389/fspas.2023.1096595>
- Ripoll, J.-F., Thaller, S., Hartley, D., Cunningham, G. S., Pierrard, V., Kurth, W., et al. (2022). Statistics and empirical models of the plasmasphere boundaries from the Van Allen Probes for radiation belt physics. *Geophysical Research Letters*, *49*, e2022GL101402. <https://doi.org/10.1029/2022GL101402>
- Schäfer, S. K. H., Glassmeier, P. T. I., Eriksson, P. N., Mager, V., Pierrard, K., Fornaçon, H., & Blomberg, L. G. (2008). Spatio-temporal structure of a poloidal Alfvén wave detected by Cluster adjacent to the dayside plasmopause. *Annales Geophysicae*, *26*(7), 1805–1817. <https://doi.org/10.5194/angeo-26-1805-2008>
- Chunk, R. W., Sojka, J. J., & Bowline, M. D. (1986). Theoretical study of the electron temperature in the high-latitude ionosphere for solar maximum and winter conditions. *Journal of Geophysical Research*, *91*(A11), 12041–12054. <https://doi.org/10.1029/JA091iA11p12041>
- Sheeley, B. W., Moldwin, M. B., Rassoul, H. K., & Anderson, R. R. (2001). An empirical plasmasphere and trough density model: CRRES observations. *Journal of Geophysical Research*, *106*(A11), 631–641. <https://doi.org/10.1029/2000JA000286>
- Verbanac, G., Bandic, M., Pierrard, V., & Cho, J. (2018). MLT plasmopause characteristics: Comparison between THEMIS observations and numerical simulations. *Journal of Geophysical Research: Space Physics*, *123*, 2000–2017. <https://doi.org/10.1002/2017JA024573>
- Verbanac, G., Pierrard, V., Bandic, M., Darrouzet, F., Rauch, J.-L., & Décréau, P. (2015). Relationship between plasmopause, solar wind and geomagnetic activity between 2007 and 2011 using Cluster data. *Annales Geophysicae*, *33*(10), 1271–1283. <https://doi.org/10.5194/angeo-33-1271-2015>
- Yahnin, A. G., Yahnina, T. A., Frey, H., & Pierrard, V. (2013). Sub-oval aurora spots: Mapping relatively to plasmopause. *Journal of Atmospheric and Solar-Terrestrial Physics*, *99*, 61–66. <https://doi.org/10.1016/j.jastp.2012.09.018>